Electrochimica Acta 559 (2026) 148623

Contents lists available at ScienceDirect

Electrochimica Acta

journal homepage: www.journals.elsevier.com/electrochimica-acta

Selective electrochemical CO_2 reduction to formate at industrial current densities using 2D $Bi_2O_2CO_3$ nanosheets

Mateus J. Tomas [a,b], Daniel R. Sevene [a,c], Gonçalves J. Marrenjo [a,d], Cleiton P.M. Silva [a], Jessica A. de Oliveira [e,f], Caue Ribeiro [f], Osmando F. Lopes [a,*]

[a] Institute of Chemistry, Federal University of Uberlândia, Campus Santa Mônica, Avenida João Naves de Avila, 2121, 34800-902 Uberlândia, Minas Gerais, Brazil
[b] Department of Tecnology and Sciences, Licungo University, Avenida Julis Nyerere, Zambezia, Estrada Regional n 642, Campus de Murrôpuè, Mozambique
[c] Department of Tecnology and Sciences, Pungue University, Tete, Campus Universitário de Cambinde - EN106, Matundo, Tete, Provincia de Tete, Mozambique
[d] Department of Natural Sciences, Save University, FPLM Avenida FPLM, 111 Inhambane, Mozambique
[e] Department of Chemistry, Federal University of São Carlos, Rod. Washington Luís Km 235, SP-310, São Carlos, São Paulo, Brazil
[f] Embrapa Instrumentation, Rua XV de Novembro, 1452 – CP 741, 13560-970 São Carlos, São Paulo, Brazil

ARTICLE INFO

Keywords:
CO_2 electroreduction
$HCOO^-$ production
Bismuth-based catalysts
Gas diffusion electrodes
Hydrothermal synthesis

ABSTRACT

Electrochemical CO_2 reduction to formate ($HCOO^-$) represents an efficient strategy to mitigate CO_2 emissions while producing value-added chemicals. However, the reaction typically requires high overpotential and suffers from low selectivity and current density. This work reports the development of $Bi_2O_2CO_3$ (BOC) nanosheets synthesized hydrothermally with urea at 90 °C (BOC-90) and 150 °C (BOC-150), evaluated in a flow-cell configuration with gas diffusion electrodes. A $Bi_2O_2CO_3$ sample calcined at 400 °C (Bi_2O_3–400) was also investigated for comparison. Both BOC-90 and BOC-150 outperformed Bi_2O_3–400 and a commercial BOC sample in $HCOO^-$ production. Notably, BOC-150 achieved a current density of -140 mA cm^{-2} and a Faradaic efficiency (FE) of 95% for $HCOO^-$ at -1.2 V vs. RHE in 0.5 M KOH. Optimizing the electrolyte concentration (1.0 M KOH) and electrode composition (75% BOC-150, 25% carbon black) further enhanced performance, yielding -250 mA cm^{-2} with FE for $HCOO^-$ (FE_{HCOO^-}) above 90%. EIS showed that BOC-150 has the lowest charge-transfer resistance, while ECSA measurements confirmed its highest active surface area, jointly explaining its enhanced ECR performance. NIR and XPS analyses revealed that strongly adsorbed water and Bi dissolution reduced BOC-90 stability, while BOC-150 maintained structural integrity and favorable surface composition. The electrode exhibited stable operation for 6 h, maintaining a Faradaic efficiency above 80% throughout the electrolysis. These findings demonstrate that BOC nanosheets, particularly those obtained under optimized hydrothermal conditions, are highly efficient and durable electrocatalysts for CO_2 reduction to $HCOO^-$ under industrially relevant conditions.

1. Introduction

The intensification of global energy consumption, historically sustained by the burning of fossil fuels, has caused a concerning increase in the atmospheric concentration of carbon dioxide (CO_2), the main greenhouse gas responsible for global warming [1–10]. Faced with this environmental challenge, the electrochemical CO_2 reduction (ECR) emerges as a promising route, allowing the conversion of CO_2 into value-added chemical compounds such as HCOOH/$HCOO^-$, carbon monoxide (CO), methane (CH_4), methanol (CH_3OH), and ethylene (C_2H_4) using electricity, preferably from renewable sources, as an energy input [10–17]. Among these products, $HCOO^-$ stands out for its industrial value, versatility as a chemical feedstock, and potential as an energy carrier in fuel cells [18].

However, the high thermodynamic stability of the CO_2 molecule poses significant challenges to its electrochemical conversion. The ECR process requires the formation of the radical anion $CO_2^{\cdot-}$, a highly unstable intermediate, which demands considerable overpotentials, significantly more negative than the theoretical potentials and favors parasitic reactions, especially hydrogen evolution reaction (HER) [2,10,19–26].

Various materials have been explored as catalysts for ECR, including

* Corresponding author.
E-mail address: osmando@ufu.br (O.F. Lopes).

https://doi.org/10.1016/j.electacta.2026.148623
Received 7 November 2025; Received in revised form 12 February 2026; Accepted 5 March 2026
Available online 6 March 2026

metals, metal oxides and molecular complexes. Among them, p-block metals-based electrocatalysts, such as bismuth (Bi), tin (Sn), lead (Pb), and indium (In), stand out for their high selectivity towards $HCOO^-$ formation [17,25–27]. However, the practical use of Pb and In based catalysts is hindered by significant drawbacks: Pb presents high toxicity and environmental hazards, while, In suffers from scarcity and high cost, which limit large-scale applications. Sn based electrocatalysts exhibit remarkable activity and selectivity for $HCOO^-$ production, but their stability under prolonged operation remains a critical challenge due to surface restructuring and dissolution phenomena [6,7,28]. Among these metals, Bi has emerged as a particularly attractive candidate owing to its low toxicity, environmental benignity, and high selectivity towards $HCOO^-$. Nevertheless, conventional Bi based catalysts still face important limitations, including low electrical conductivity, restricted surface area, and intrinsically low exposure of active sites, which result in modest catalytic activity, especially under severe operating conditions [22,29].

The challenges described above highlight the critical need to advance catalytic systems for the ECR. To address several limitations described, a promising approach involves the use of two-dimensional (2D) nanostructures, such as bismuth oxycarbonate (BOC) nanosheets. These materials offer a significantly higher surface to volume ratio, thereby increasing the density of catalytically active sites. Furthermore, their integration into gas diffusion electrodes (GDEs) within flow cell reactors is crucial, as this configuration overcomes mass transport limitations and allows for operation at industrially relevant current densities, while also facilitating the suppression of the competing HER (>200 mA cm^{-2}) [22,30–34].

Therefore, in this work, we aim to develop and evaluate 2D bismuth oxycarbonate ($Bi_2O_2CO_3$, BOC) nanostructures synthesized under controlled hydrothermal conditions as efficient electrocatalysts for the CO_2 reduction reaction to $HCOO^-$. The synthesized materials will be characterized and applied in a electrochemical flow cell equipped with gas diffusion electrodes to assess their catalytic activity, selectivity, and stability under conditions relevant to industrial applications. Additionally, the influence of synthesis temperature and structural transformation to Bi_2O_3 on the electrochemical performance will be systematically investigated. Through this approach, we seek to establish structure activity relationships and elucidate the factors governing the superior performance of BOC nanosheets, contributing to the rational design of next generation bismuth based catalysts for efficient and selective CO_2 electroreduction to $HCOO^-$.

2. Materials and methods

2.1. Synthesis of $Bi_2O_2CO_3$ and Bi_2O_3 samples

$Bi_2O_2CO_3$ was synthesized via a hydrothermal method [35]. 6.066 g of urea $(NH_2)_2CO)$] was dissolved in 40 ml of methanol (CH_3OH), while 0.97014 g of $Bi(NO_3)_35H_2O$ was dissolved in 40 mL of deionized water. Then, both solutions were mixed and stirred at room temperature for 30 min, then transferred to a Teflon-lined autoclave and treated hydrothermally at 90, 150 °C for 240 min with a heating rate of 5 °C/min. After hydrothermal treatment, the products were washed three times (10 min each) and dried at 70 °C for 12 h. The sample treated at 90 and 150 °C were denoted as BOC-90 and BOC-150, respectively. For comparison, BOC-90 was annealed at 400 °C to obtain Bi_2O_3, denoted as Bi_2O_3–400. Commercial $Bi_2O_2CO_3$ powder (Sigma-Aldrich) (denoted as BOCCOM) was used as a reference material in all structural, physicochemical, and electrochemical analyses.

2.2. Preparation of gas diffusion electrodes

Gas diffusion electrodes were prepared by spray coating onto a carbon paper substrate (GDL-Sigracet, 39B) using an airbrush (Vonder). The ink was composed of 7.5 mg of catalyst (BOC or Bi_2O_3), 7.5 mg of carbon black (amorphous carbon, CAS #1333–86–4), 17 μL of an ionomer (*Sustainion XA-95% in Ethanol, Dioxide Materials Inc.*), 1 mL of deionized water, and 1 mL of isopropanol (Vetec 99.5%). Different weight ratios of the electrocatalyst and carbon black were evaluated: 25, 50 and 75%. The mixture was placed in a 10 mL beaker within a cold water bath and then subjected to 30 min of sonication using an ultrasonic tip sonicator (Sonics & Materials INC, VCX130) with a power of 130 W. Subsequently, the homogenized solution was uniformly deposited onto a 16 cm^2 area of carbon paper using an airbrush and then dried in an oven at 80 °C for 24 h. The prepared electrodes exhibited a loading of 0.19 mg cm^{-2}. Finally, a 1 cm^2 piece of the electrode was cut and applied as the working electrode for the ECR.

2.3. Materials characterization

The crystalline structure of the synthesized materials was investigated using X-ray diffraction (*XRD*) with a Shimadzu XRD600 powder diffractometer operating at 40 kV and 30 mA, employing Cu Kα radiation. Data were collected over a 2θ range of 10° to 70° with a scan rate of 0.02° min^{-1}. Crystallite size information was extracted from the XRD patterns and calculated using the Scherrer equation (Eq S1). The short range structure of the BOC samples was characterized by Raman spectroscopy using a HORIBA LabRAM HR Evolution confocal spectrometer equipped with a customized CCD detector (OSD Syncerity) and four laser lines, operated with HORIBA Scientific's LabSpec software. A 532 nm excitation laser was employed, delivering 50 mW at the sample (corresponding to 78 mW before the objective), as measured with a power meter. Attenuated total reflectance Fourier-transform infrared (ATR FTIR) spectra were recorded using a PerkinElmer Frontier spectrometer with a diamond crystal, to identify the functional groups present in the samples. Measurements were performed with 128 scans and a resolution of 4 cm^{-1} over the range of 200 to 2400 cm^{-1}.

The surface morphology of the materials was characterized by field emission scanning electron microscopy *(FEG SEM)* using a JEOL 6701F instrument. For sample preparation, small amounts of the powders were individually suspended in isopropanol, drop-cast onto Si substrates, and subsequently mounted on stubs with carbon tape for imaging of BOC and Bi_2O_3.

Thermogravimetric analysis (*TGA*) was performed using a Shimadzu DTG-60H instrument to evaluate the thermal stability and compositional changes of both the synthesized and commercial samples as a function of temperature. The analysis was conducted on a sample weight of 10 mg under a synthetic air flow of 50 mL min^{-1}, with a heating rate of 10 °C min^{-1} over a temperature range of 30 to 600 °C. The specific surface area of the samples was determined by nitrogen (N_2) physisorption at 77 K using a Micromeritics ASAP 2000 instrument (Norcross, Georgia, USA). The Brunauer-Emmett-Teller (BET) model was applied to estimate the surface area. Prior to the measurements, the samples were degassed at 80 °C under vacuum until a pressure below 10 μmHg was achieved. Near-infrared spectroscopy (NIR) was employed to assess the surface coverage of OH^- groups on the samples by qualitatively determining the adsorption of water molecules, using a PerkinElmer Spectrum 100 spectrometer. X-ray photoelectron spectroscopy (XPS) was employed to determine the chemical states of the synthesized BOC samples. The measurements were carried out on a Scienta Omicron ESCA+ spectrometer equipped with a high-performance EA 125 hemispherical analyzer, using monochromatic Al Kα radiation ($h\nu = 1486.6$ eV) as the excitation source. During data acquisition, the ultra-high vacuum chamber was maintained at a base pressure of 2×10^{-9} mbar. Survey spectra and high-resolution spectra were collected with energy steps of 0.50 eV and 0.05 eV, respectively. Quantitative analysis was performed using the O 1 s, C 1 s, F 1 s, and Bi 4f core levels. The binding energy scale was calibrated by setting the C–C component of the adventitious carbon C 1 s peak to 284.8 eV. Spectral deconvolution was performed in CasaXPS software using Shirley and Tougaard background subtraction, with peak fitting based on mixed Gaussian-Lorentzian

functions.

2.4. ECR performance evaluation

All electrochemical measurements were performed on a potentiostat/galvanostat (*Autolab PGSTAT204, Metrohm*). The ECR experiments were carried out in a commercial flow cell (Micro Flow Cell, Electrocell) with three compartments. BOC and Bi_2O_3-based electrodes with 1 cm^2 were used as working electrodes, nickel foam as the counter electrode, a leak-free Ag/AgCl (3 M) as the reference electrode, and an anion exchange membrane (FAB-PK-130, Fumasep) to separate the cathode and anode. KOH solutions at different concentrations (0.5 to 2.0 mol L^{-1}) were used as the electrolyte and circulated through the cell using a peristaltic pump at a flow rate of 6 mL min^{-1}. CO_2 (99.99%) was purged through the back and across the GDE at a flow rate of 30 mL min^{-1}, controlled by a rotameter (Aalborg, Orangeburg). The electrochemical performance was evaluated from the material linear sweep voltammetry (LSV) in the potential window of −0.4 to −1.2 V vs RHE. Potentials were converted to the RHE scale using the following equation:

$$E\ (V\ vs\ RHE) = E\ (V\ vs\ Ag/AgCl) + 0.197\ V + 0.0592 \times pH$$

Electrolysis was performed at different applied potentials (−0.8, −1.0, and −1.2 V vs. RHE), with the gaseous and liquid products of the reaction being analyzed every 30 min. To investigate the electrode stability, chronopotentiometry experiment was performed at a constant current of −40 mA for 6 h. The potential and FE was monitored throughout the experiment to evaluate operational stability under steady-state conditions. For the stability experiment the catalyst was deposited onto a PTFE-based gas diffusion electrode (GDE), which was used as the cathode, to overcome the flooding problem.

The gaseous products exiting the cell were transported by the continuous CO_2 flow to a gas collection bag, where aliquots were collected with a syringe and injected into a gas chromatograph equipped with a thermal conductivity detector (GC-TCD, PerkinElmer Clarus 580) for quantification of CO and H_2 concentrations.

$HCOO^-$ quantification was performed by high-performance liquid chromatography (HPLC) using a Shimadzu system, operated with LabSolutions software. Samples were prepared from 5 mL aliquots of electrolyte, adjusted to pH 2.0, filtered through a 0.22 μm syringe filter, and transferred into vials. Separation was carried out on an Aminex HPX-87H column (Bio-Rad), maintained at 60 °C, using 2.5 mmol L^{-1} H_2SO_4 as the mobile phase under isocratic mode and pumped at a flow rate of 0.7 mL min^{-1}. Detection was performed at 210 nm, with $HCOO^-$ identification confirmed by comparing retention times with authentic standards. Quantification was achieved by integrating the peak area and interpolating against a calibration curve constructed from standard solutions of known concentrations.

The FE was determined by the following equation:

$$FE = \frac{2\ n\ F}{Q} x100\%$$

Where 2 is the number of electrons involved in the reaction, n is the number of moles of the product $HCOO^-$ or H_2 calculated according to HPLC and GC data, respectively. F is the Faraday constant, with a value of 96,485 C mol^{-1} and Q is the total charge passed during the electrolysis.

The partial current density (j_{HCOO-}) was calculated according to the equation:

$$j_{HCOO-} = j\ x\ FE$$

where j is the total current density and FE is the Faradaic efficiency for $HCOO^-$. This parameter reflects the effective current density associated specifically with $HCOO^-$ production, providing a direct measure of the catalytic activity toward the target product.

3. Results and discussion

3.1. Characterization of the $Bi_2O_2CO_3$ samples

The XRD patterns of the synthesized samples (BOC-90, BOC-150, and Bi_2O_3–400) were obtained to evaluate their crystalline phase and degree, and to compare them with the commercial BOC (Fig. 1**a**). The hydrothermally treated $Bi_2O_2CO_3$ samples displayed a typical XRD pattern attributed to the tetragonal crystalline phase (PDF No 041–1488) with no detectable secondary phases, similar to the commercial BOC [10,36,37]. Bi_2O_3–400 sample exhibits all the peaks corresponding to the α-Bi_2O_3 phase (PDF No 01–071–2274) with the presence of the main peak of $Bi_2O_2CO_3$, which indicates that the thermal treatment was not able to completely convert the BOC into Bi_2O_3 [38]. Hydrothermal synthesis at low temperatures (90 °C and 150 °C) led to the formation of phase pure $Bi_2O_2CO_3$, albeit with distinct degrees of crystallinity. The sample synthesized at 90 °C exhibited broader XRD peaks, indicating lower crystallinity degree/reduced crystallite size compared to the sample synthesized at 150 °C. Conversely, the calcined sample (Bi_2O_3–400) presented sharper and more intense diffraction peaks relative to the hydrothermally synthesized samples, evidencing enhanced crystallinity as a result of the thermal treatment [37–40].

TGA analysis (Fig. 1**b**) exhibits mass losses that occur due to processes such as dehydration, decomposition, and volatilization. The synthesized samples of BOC-90, BOC-150, and BOCCOM show several stages of mass loss. The first stage, at low temperatures (below 200 °C), is attributed to the loss of adsorbed water and other volatile species adsorbed on the samples surface. The second stage, at higher temperatures (between 200 °C and 400 °C), corresponds to the decomposition of carbonate groups and the release of CO_2. The differences in the intensities and temperatures of the mass loss stages indicate changes in the sample's crystallinity degree, composition, and the presence of impurities [3,36,41]. Bi_2O_3–400 sample exhibit greater thermal stability, due to the decomposition of the carbonate and formation of Bi_2O_3. The commercial sample serves as a reference to comparing the thermal properties of the synthesized and calcined samples.

The detailed analysis of Raman and ATR-FTIR spectra of the synthesized $Bi_2O_2CO_3$ samples revealed crucial information about the short-range structure and the presence of the functional groups on the materials surface, respectively. The Raman spectra, presented in Fig. 1**c**, demonstrated the typical behavior of $Bi_2O_2CO_3$ for all synthesized samples, except the calcined one. Characteristic bands were identified at 1063 cm^{-1}, attributed to the symmetric stretching of the CO_3^{2-} ion, and below 400 cm^{-1}, corresponding to the vibrational modes of Bi-O bonds. The similarity of the profiles of the synthesized samples with that of the commercial $Bi_2O_2CO_3$ sample suggests a comparable short-range structure. The lower intensity of the peaks in BOC-90 and BOC-150, compared to BOCCOM, suggests a lower crystallinity in these samples, as observed by XRD. The Raman spectrum of the Bi_2O_3–400 showed the disappearance or weakening of peaks associated with C—O bonds (specifically the 1063 cm^{-1} peak of CO_3^{2-}) and the appearance of characteristic peaks of the Bi-O bonds present in Bi_2O_3. Specifically, the observed peaks at 120, 214, 317, and 447 cm^{-1} are in good agreement with the literature for the monoclinic α-Bi_2O_3 phase. The intensity and sharpness of these bands indicate a high degree of crystallinity [4,36,42].

ATR-FTIR analysis (Fig. 1**d**) reveals characteristic bands primarily associated with Bi-O vibrations, confirming the structural evolution of the samples as a function of thermal treatment. For the BOCCOM sample, an absorption band at 1740 cm^{-1} is assigned to the $C = O$ stretching vibration, while the typical vibrational modes of CO_3^{2-} appear at 1370 cm^{-1} (antisymmetric stretching, v_3), 1066 cm^{-1} and 670 cm^{-1} (symmetric stretching, v_1, and in-plane bending, v_4, respectively), and at 843 cm^{-1} (out-of-plane bending, v_2), clearly indicating the formation of $Bi_2O_2CO_3$. These signals can be observed for the samples treated at 90 and 150 °C, which confirm the formation of $Bi_2O_2CO_3$ as observed by XRD and

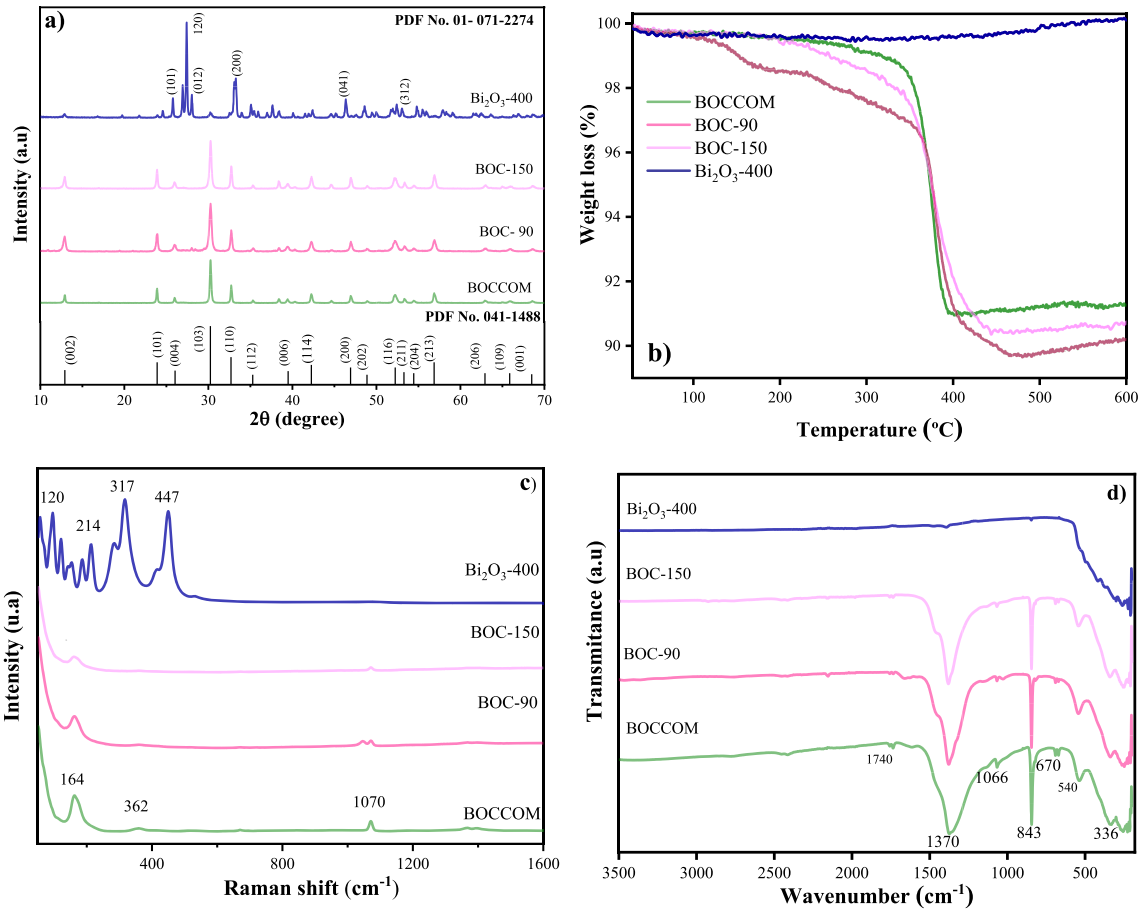

Fig. 1. a) XRD patterns b)TGA analysis **c)** Raman scattering spectra and **d)** ATR-FTIR spectra of the BOCCOM, BOC-90, BOC-150, and Bi_2O_3–400 samples.

Raman analyses. In contrast, the sample calcined at 400 °C (Bi_2O_3–400) no longer exhibits carbonate-related bands, being dominated by broad absorptions below 500 cm^{-1} that are attributed to Bi-O vibrations, thereby confirming the complete conversion of $Bi_2O_2CO_3$ into Bi_2O_3, in agreement with TGA and Raman data [36,42,4,43]. It is important to note that although FTIR spectra suggest complete decomposition of carbonate species at 400 °C, XRD analysis reveals a small residual crystalline fraction of $Bi_2O_2CO_3$, which can be attributed to the higher sensitivity of XRD to minor crystalline phases compared to FTIR.

The material's morphology was investigated by SEM, illustrated in Fig. 2. The hydrothermal synthesis carried out at low temperatures (90 °C and 150 °C) resulted in the formation of particles with varied morphologies, including nanosheets and microspheres. The particles synthesized at these temperatures exhibited micrometric sizes and nanometric thicknesses, where the sample BOC-90 exhibited particle size smaller than BOC-150. In contrast, the sample calcined at 400 °C exhibits relatively larger sizes, characterized by agglomerated particles. Additionally, it can be observed that BOC-90 and BOC-150 exhibited particle size smaller than the commercial sample.

The analysis of N_2 adsorption–desorption isotherms using the Brunauer–Emmet Teller (BET) method for the BOC-90, BOC-150, Bi_2O_3–400, and BOCCOM samples (Fig. S1) reveals significant differences in their specific surface areas (SSA), pore volumes, and average pore sizes (Table 1). The Bi_2O_3–400 sample exhibited the largest surface area (30.86 m^2 g^{-1}) and the highest pore volume (0.06 cm^3 g^{-1}). Although its average pore size (3.04 nm) is intermediate, the combination of high area and volume indicates a well-developed and accessible porous structure. The BOCCOM sample served as a reference point for the lowest porosity in this study. With the smallest surface area (11.96 m^2 g^{-1}) and the lowest pore volume (0.015 cm^3 g^{-1}), in addition to a very reduced pore size (1.92 nm), BOCCOM suggests a less porous and less accessible structure for nitrogen adsorption. The BOC-90 and BOC-150 samples exhibit intermediate characteristics but with important distinctions. BOC-90 exhibits a SSA value of 21.6 m^2 g^{-1}, 0.048 cm^3 g^{-1} of pore volume, and 3.59 nm pore size, demonstrating considerable porosity that surpasses BOCCOM in all aspects. BOC-150 exhibits a smaller surface area (7.4 m^2 g^{-1}) than BOCCOM, while it compensates with a larger pore volume (0.029 cm^3 g^{-1}) and, notably, the largest pore size (6.83 nm) among all samples. This characteristic suggests a structure with wider pores, which can be advantageous for the diffusion or adsorption of larger molecules that would not be able to access smaller pores [44–47].

3.2. *Electrocatalytic performance of BOC samples for ECR*

The electrocatalytic performance of BOC samples for CO_2 reduction were analyzed by LSV curves and by electrolysis experiments at different applied potential (chronoamperometry) to assess the selectivity for $HCOO^-$ production (FE_{HCOO^-}). A comparative analysis of the results (Fig. 3) revealed distinct catalytic activities among the evaluated materials under the same reaction conditions. The Bi_2O_3-based sample, calcined at 400 °C, showed the lower performance for $HCOO^-$ production, with a current density of approximately 90 mA cm^{-2} (Fig. 3**a**) and a FE_{HCOO^-} of about 72% at −1.2 V vs. RHE, using a 0.5 M KOH electrolyte (Fig. 3**b**). The synthesized BOC samples demonstrated superior performance in the conversion of CO_2 to $HCOO^-$. The BOC-90 catalyst exhibited a current density of approximately −125 mA cm^{-2} and a FE_{HCOO^-} of 94% under the same conditions. Notably, the BOC-150 catalyst stood out as the most promising among the synthesized samples, achieving a current density of −140 mA cm^{-2} and FE_{HCOO^-} of 95% at

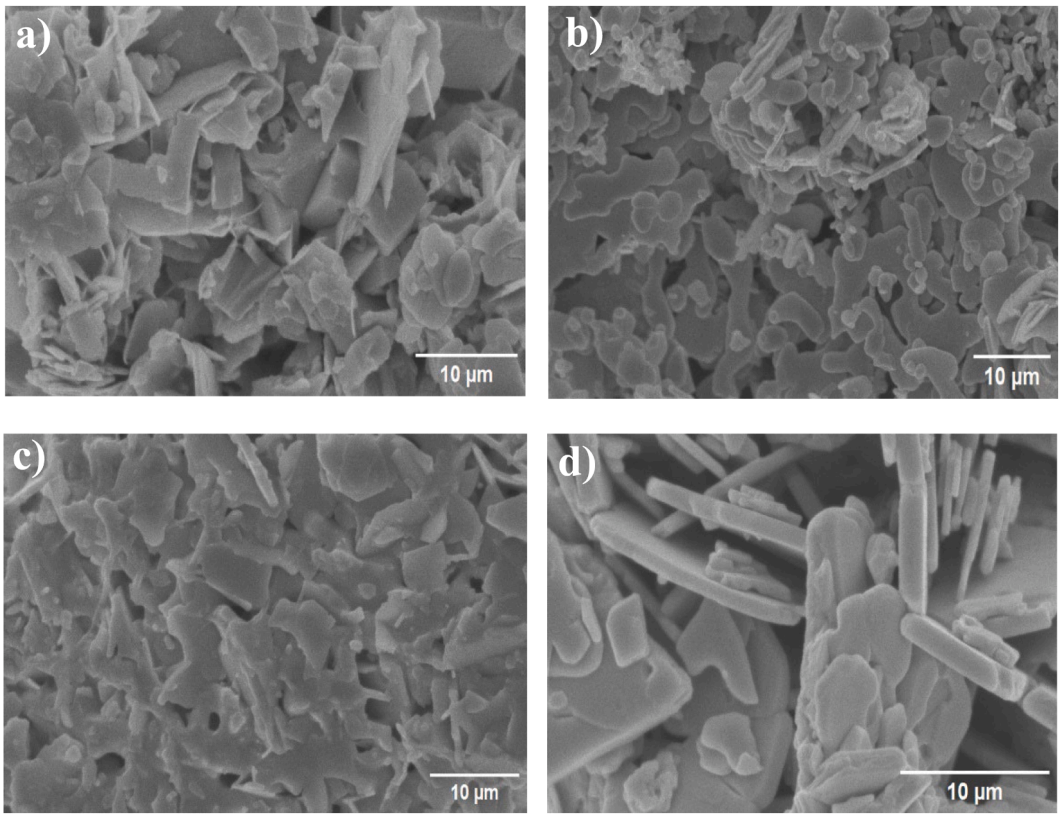

Fig. 2. SEM images of the synthesized samples **(a)** BOC-90, **(b)** BOC-150, **(c)** Bi_2O_3–400, and **(d)** BOCCOM.

Table 1
Nitrogen adsorption-desorption data of the BOC-90, BOC-150, Bi_2O_3–400, and BOCCOM samples.

Samples	SSA (m^2g^{-1})	Pore volume ($cm^3\ g^{-1}$)	Pore size (nm)
BOC-90	22	0.05	3.6
BOC-150	7	0.03	6.8
Bi_2O_3–400	31	0.06	3.0
BOCCOM	12	0.02	1.9

the same potential and electrolyte concentration. These results confirm the effectiveness of the 2D materials approach, which, according to the literature, substantially increases current density [48]. The high FE for $HCOO^-$, greater than 90%, is consistent with expectations for Bi based electrocatalysts [42,49]. The commercial BOC material presented a current density of about −100 mA cm^{-2} and a FE_{HCOO^-} of 78% at a potential of −1.2 V vs. RHE. This evidence the effectiveness of the synthesis methodology employed in this study for obtaining BOC catalysts with enhanced catalytic performance and greater selectivity to produce $HCOO^-$ from CO_2 reduction compared to the commercial material, in a flow-cell system with gas diffusion electrodes.

Additionally, the carbon paper used as the gas diffusion electrode substrate was systematically evaluated by both LSV and 30 min chronoamperometry experiments under identical conditions to those applied for the BOC electrodes (Fig. 3). In the LSV curves, the bare carbon paper exhibited a significantly lower current density, reaching approximately $-50\ mA.cm^{-2}$ at −1.2 V vs RHE, which is markedly inferior to that obtained for the synthesized BOC samples. More importantly, product analysis after electrolysis revealed that, in the absence of BOC samples, no $HCOO^-$ or any other carbon-containing product was detected in either the liquid or gas phase. The only product identified by GC-TCD was H_2, with a Faradaic efficiency of 100% within experimental accuracy at all investigated potentials. Because no formate was formed on the bare substrate, these data were not included in Fig. 3b, which focuses on formate production.

These control experiments clearly demonstrate that the carbon paper itself does not exhibit intrinsic activity toward ECR and acts solely as an HER-active conductive support under the studied conditions. Therefore, the selective formation of $HCOO^-$ observed in the catalyst-coated electrodes can be unequivocally attributed to the intrinsic catalytic properties of the BOC and Bi_2O_3 phase, ruling out any contribution from the gas diffusion substrate to the reported activity and selectivity.

Electrochemical impedance spectroscopy (EIS) measurements were performed before and after electrolysis in order to evaluate possible interfacial and structural reconstruction effects induced under cathodic operation. The EIS results recorded prior to the electrolysis (Fig. 4**a-b**) reveal clear differences in the area-normalized charge-transfer resistance (R_{ct}) among the samples investigated. As we can see in Table S2, the higher R_{ct} observed for BOC-90 and BOCCOM suggests more hindered electron-transfer kinetics, which may be associated with lower electrical conductivity and/or the presence of surface species formed during the milder hydrothermal synthesis conditions. In contrast, BOC-150 exhibited the lowest R_{ct} value, consistent with its superior ECR performance [23].

After electrolysis at −1.0 V vs RHE for 10 min (Fig. 4**c–d**), a decrease in R_{ct} was observed for all samples. This behavior is expected, since partial reduction of Bi^{3+} to metallic Bi under cathodic polarization can increase the electrical conductivity of the catalyst surface. Under these conditions, BOC-150 maintained the lowest R_{ct} (followed by BOCCOM, Bi2O3–400, and BOC-90 (Table S2 and S3). The consistently lower R_{ct} of BOC-150 indicates more favorable interfacial charge-transfer kinetics under operational conditions, in agreement with previous reports correlating reduced R_{ct} values with enhanced electrocatalytic performance [50]. Additionally, BOC-150 displays the highest constant phase element (CPE) value, suggesting a larger effective interfacial capacitance, which is typically associated with a higher electrochemically

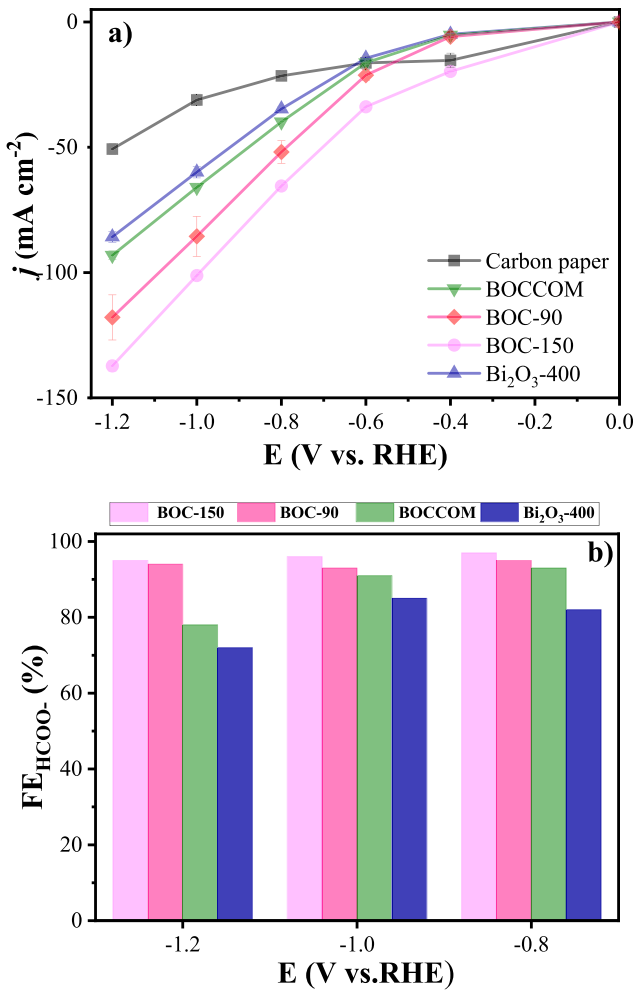

Fig. 3. **(a)** LSV curves for carbon paper and BOC samples in 0.5 M KOH electrolyte in a electrochemical flow cell, applying potential range of −0.4 to −1.2 vs. RHE. **(b)** FE_{HCOO^-} obtained at corresponding applied potential (−0.8 to −1.2 V) during 30 min. Carbon paper is not included in panel (b) because no HCOO- production was detected.

active surface area and improved electrode–electrolyte interaction [51]. Overall, although reconstruction occurs under cathodic polarization, the comparable impedance features before and after electrolysis and the consistently lower R_{ct} of BOC-150 confirm its superior charge-transfer properties, which directly contribute to its improved catalytic performance.

The evaluation of ECSA through cyclic voltammetry is essential to rationalize the catalytic performance, since a larger electrochemically accessible surface correlates with higher activity in CO_2 reduction. This ECSA was estimated by calculating the double-layer capacitance (C_{dl}), as shown in Fig. 5, from the current response obtained at different scan rates (Fig. S2). The synthesized samples (BOC-90, BOC-150, Bi_2O_3–400) exhibited higher C_{dl} values compared to the BOCCOM sample, evidencing the effectiveness of structural modification and thermal treatments. Among them, BOC-90 presented the largest ECSA, attributed to a more favorable morphology and phase composition that increased surface area and electroactive sites. BOC-150 also showed an enhanced ECSA relative to the reference, though slightly lower than BOC-90, which may be associated with partial agglomeration or pore collapse induced by higher temperature treatment, in agreement with SSA analysis. Bi_2O_3–400 displayed improved ECSA compared to BOCCOM, but lower than the BOC samples, indicating that excessive crystallization at elevated temperature reduced surface area and ion accessibility. These results confirm that moderate treatments, such as 90 °C, provide the most suitable balance between crystallinity and surface exposure, explaining the superior catalytic performance of BOC-90 and BOC-150 in ECR [24,25].

The XPS analysis (Fig. 6a) revealed significant differences between the BOC-90 and BOC-150 samples before and after the ECR. High-resolution spectra (Fig. S3 a, b and c) indicated a higher proportion of Bi^{2+} species and oxygen vacancies in the BOC-90 powder (Fig. S3), which remained nearly unchanged after the reaction, suggesting partial poisoning of these sites. In contrast, BOC-150 exhibited complete surface oxidation to Bi^{3+} during electrocatalysis, evidencing active surface reconstruction and improved accessibility of catalytic sites. This process explains its higher FE and partial current density for $HCOO^-$, even with a lower surface area and porosity compared to BOC-90. It can be observed that the bismuth signals decreased dramatically for BOC-90 after the ECR, indicating that this sample exhibits low stability, probably due to a cathodic dissolution process. In contrast, the BOC-150 sample retained a significant amount of bismuth on the electrode surface after the reaction, which explains its higher catalytic activity. Additionally, the F 1s signals (Fig. S4) can be ascribed to the carbon paper substrate, which exhibits hydrophobic characteristics because of the PTFE treatment. This feature becomes particularly pronounced for the BOC-90 sample after the ECR, likely due to the exposure of the carbon paper surface following Bi leaching into the electrolyte. These findings corroborate that surface reconstruction ability and the regeneration of active Bi^{3+} species are key factors determining the superior electrocatalytic performance of BOC-150 [52,53].

The NIR spectra of the as-synthesized powders (Fig. 6b) exhibit distinct signatures of hydroxyl species and adsorbed water, with detailed assignments provided in Table S2 (SI). Bands at 4330 and 4500 cm^{-1} are attributed to structural OH groups and lattice-bound hydroxyls [54], while features in the 4900–5200 cm^{-1} range correspond to different hydrogen-bonding states of water molecules adsorbed on the surface [55,56]. At higher energies (7000 cm^{-1}), the observed bands originate from surface hydroxyls in distinct coordination environments [55–57]. Notably, BOC-150 displayed only a broad feature near 7000 cm^{-1}, indicating the presence of weakly adsorbed hydroxyls and the absence of strongly bonded water. This unique surface state prevents site blocking and explains the superior electrocatalytic activity of BOC-150 toward CO_2 to $HCOO^-$ conversion. In contrast, BOC-90 exhibits pronounced contributions from strongly adsorbed water, which likely hinders charge transport by acting as an insulating component.

The electrolyte concentration and the ration between catalyst and carbon paper are parameters relevant in the optimization of the electrode performance for any electrocatalytic application. Therefore, both parameters were evaluated using the sample with the best performance, BOC-150, as can be seen in (Fig. 7). The current density is strongly influenced by KOH concentration. A positive correlation was observed between KOH concentration and current density, with the 2.0 M KOH electrolyte exhibiting the highest values (−185 mA cm^{-2} at −1.2 V vs. RHE). This increase can be attributed to two main factors: (i) the improvement in the ionic conductivity of the solution, which facilitates charge transport and minimizes ohmic losses; and (ii) the favoring of the formation of electroactive carbon species, such as bicarbonate, in more alkaline solutions, making them more available at the electrode-electrolyte interface for the reduction reaction [17,58,59].

Selectivity for $HCOO^-$ (Fig. 7**b**) showed strong dependence on electrolyte concentration, with the 0.5 M KOH solution being the most favorable condition, with FE of about 95% at −1.2 V vs. RHE and 80% at −0.8 and −1.0 V, in addition to high partial current density. At higher concentrations (1.0 M and 2.0 M KOH), despite the increase in total current density, selectivity was reduced, indicating that higher overall activity does not necessarily imply higher charge conversion to $HCOO^-$ [60–62]. Additionally, in alkaline systems, increasing KOH concentration can intensify OH^- ion crossover through anionic membranes, modifying the local pH at the cathode and contributing to the loss of

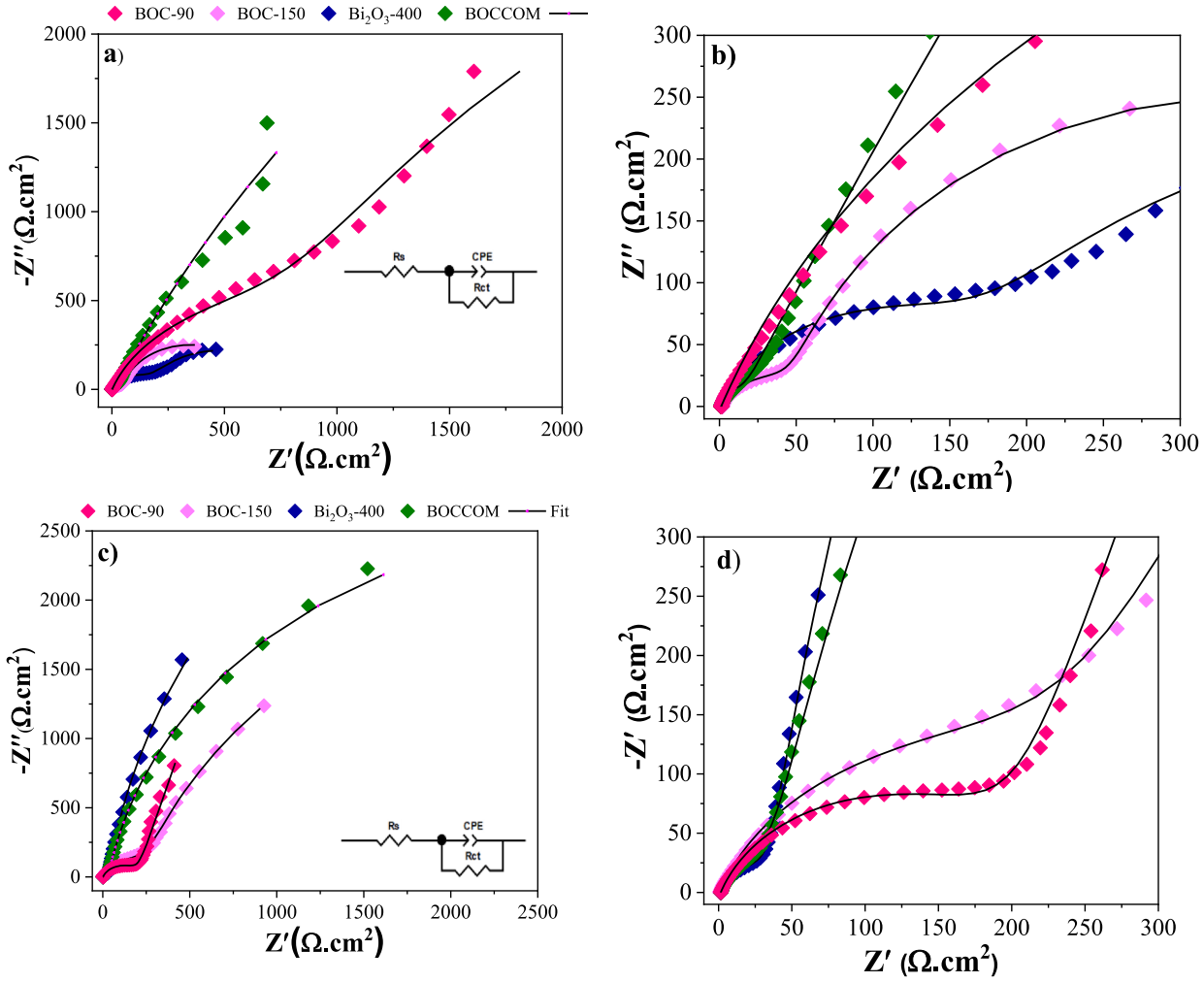

Fig. 4. Electrochemical impedance spectra of BOCCOM, BOC-90, BOC-150 and BOC-400 samples in 1.0 M KOH electrolyte (Nyquist plots); before electrolysis (A) and (B), and after electrolysis (C) and (D).

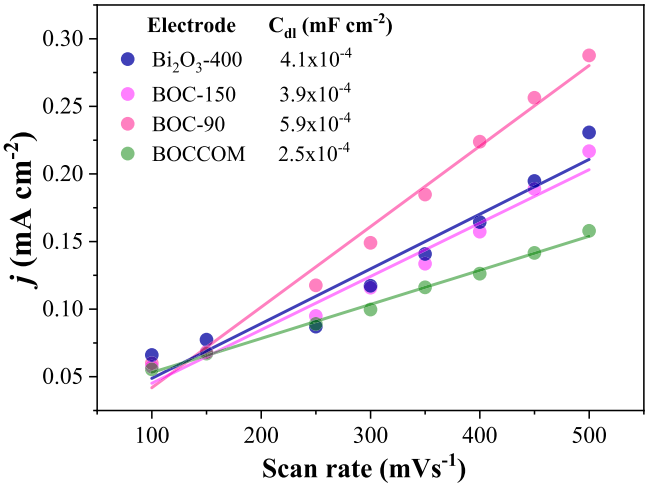

Fig. 5. Double-layer capacitance (C_{dl}) obtained by cyclic voltametry studies at different scan rates from 100 to 500 mVs^{-1} of BOCCOM, BOC-90, BOC-150 and Bi_2O_3–400 samples.

selectivity observed at high alkalinities [49,63]. In this context, the use of proton exchange membranes has been recommended to decouple the intrinsic effects of electrolyte concentration from those associated with anionic transport, allowing a more accurate assessment of the selectivity and mechanisms of ECR [49,64].

Fig. 7**c-d** showed the electrocatalytic activity of the different electrodes modified with the BOC-150 catalyst in different proportions of carbon black in a 1 M KOH. The electrode prepared with 75% of BOC-150 demonstrates the best performance in terms of current density and FE. At −1.2 V vs. RHE, this electrode achieves a current density around −250 mA cm^{-2} and FE_{HCOO^-} of about 99%. This value is superior to that obtained with 50% BOC-150 (−160 mA cm^{-2}) and 100% BOC-150 (−190 mA cm^{-2}) at the same potential. This result meets the requirement for commercially relevant current densities (>200 mA cm^{-2}) [65,66]. The 75% BOC-150 composition exhibited the best electrocatalytic performance, resulting from a favorable balance between the high density of active sites and the adequate electrical conductivity provided by carbon, as reflected in its lowest Rct value (Fig. S6). In contrast, the 50% BOC-150 formulation, although benefiting from a higher conductive fraction, is limited by the reduced number of catalytic sites, while the electrode composed of 100% BOC-150 displays an even higher Rct, highlighting the lack of efficient conductive pathways and optimal interfaces. Therefore, the 75% composition represents the most favorable condition, combining catalytic activity, conductivity, and mass transport, which ultimately leads to the highest current density.

Preliminary experiments using carbon paper as the electrode support showed satisfactory stability performance only during the initial 30 min

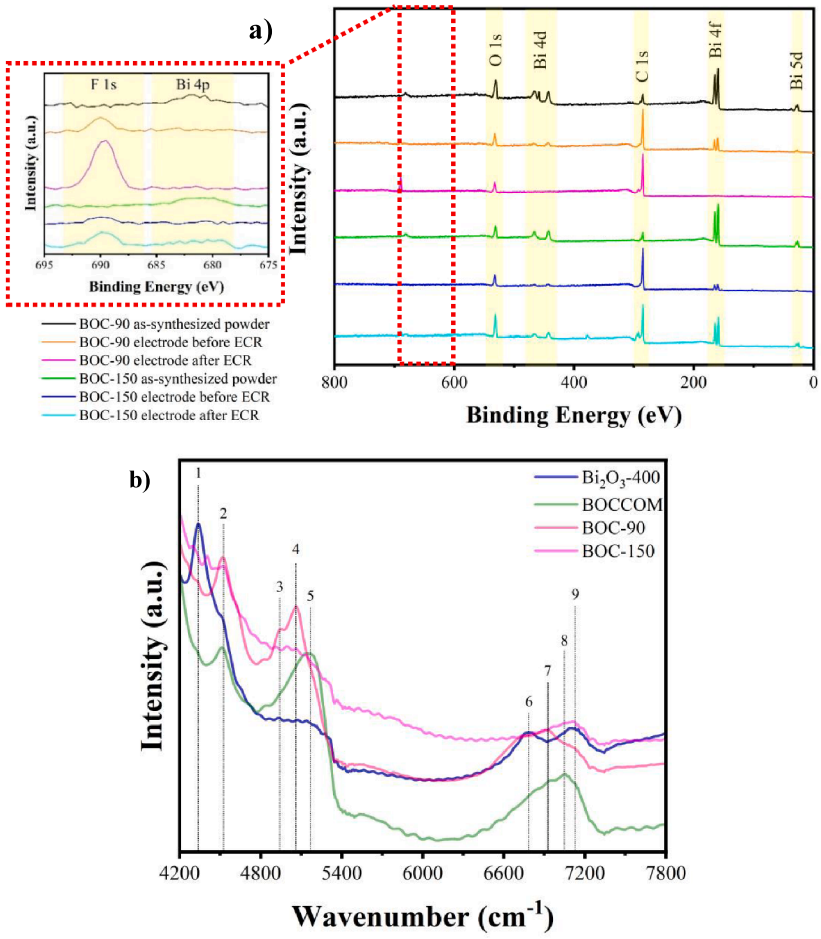

Fig. 6. a) XPS survey spectra of BOC-90 and BOC-150 powders (as-synthesized) and electrodes before and after the ECR reaction. Near-infrared spectrum (NIR) of the as-synthesized powders (Bi_2O_3–400, BOC-90, BOC-150) and commercial $Bi_2O_2CO_3$ (BOCCOM).

of operation. Subsequently, a rapid deterioration in electrochemical stability was observed, which is attributed to progressive electrode flooding, as observed by contact angle measurements (Fig. S7). This phenomenon severely restricts CO_2 mass transport to the active sites and promotes competing reactions, particularly HER, leading to potential instability and a marked decrease in FE_{HCOO^-}. Similar flooding-induced limitations in carbon-based gas diffusion electrodes under alkaline CO_2 reduction conditions have been widely reported in the literature. In contrast, when the BOC-150 catalyst was directly deposited onto a PTFE membrane, the electrochemical stability was significantly improved. Chronopotentiometric measurements conducted at a constant current of −40 mA in 0.5 M KOH demonstrated stable operation over 6 h, with the FE_{HCOO^-} remaining consistently high, predominantly in the range of 80 and 90%. The potential time profiles over the 6 h operation, as well as the stability behavior as a function of the applied current can be seen in the Fig. S8. These results clearly indicate that the stability loss observed with carbon paper does not arise from the intrinsic properties of the BOC-150 catalyst, but rather from electrode architecture related flooding effects. The PTFE based configuration effectively mitigates electrolyte accumulation, ensures efficient reactant transport, and enables sustained and selective CO_2 electroreduction under alkaline conditions.

The electrochemical stability of the BOC-150 catalyst was evaluated by chronopotentiometry at a constant current of - 40 mA for 6 h in 0.5 M KOH, using an electrode configuration in which the catalyst was directly deposited onto a PTFE membrane (Fig. 8). After a brief initial conditioning period, the electrode potential stabilized and remained nearly constant throughout the entire operation time, with no noticeable drift, indicating high electrochemical stability under alkaline conditions. The FE_{HCOO^-} remained high, around 80%, over the 6 h test, demonstrating sustained catalytic selectivity and effective suppression of competing reactions, particularly HER. The PTFE based configuration effectively mitigates electrolyte accumulation, ensures efficient reactant transport, and enables sustained and selective CO_2 electroreduction under alkaline conditions [67].

4. Conclusion

In this study, we successfully developed highly efficient and selective electrocatalysts for the ECR to $HCOO^-$ under industrially relevant conditions. BOC-150 nanosheets emerged as the superior catalyst, demonstrating the highest current density for $HCOO^-$ production. Optimizing the electrolyte concentration to 1.0 M KOH and the electrode composition to 75% BOC-150 catalyst and 25% carbon black further boosted performance, achieving an impressive current density of -250 mA cm^{-2} and a FE_{HCOO^-} higher than 90%. BOC-150 consistently showed the best overall performance in terms of both $HCOO^-$ production rate and selectivity. EIS confirmed that BOC-150 exhibited lowest charge transfer resistance, indicating favorable reaction kinetics. Complementary spectroscopic analyses provided further insight into the structure-performance relationship. NIR spectra revealed the presence of strongly adsorbed water species on the BOC-90 sample, which likely hindered CO_2 adsorption and charge transfer, explaining its inferior catalytic performance. Moreover, XPS analysis after the ECR confirmed the instability of BOC-90, evidenced by the significant decrease in bismuth signals due to partial dissolution in the electrolyte. BOC-150 prepared on PTFE membrane as GDE was stable during 6 h with

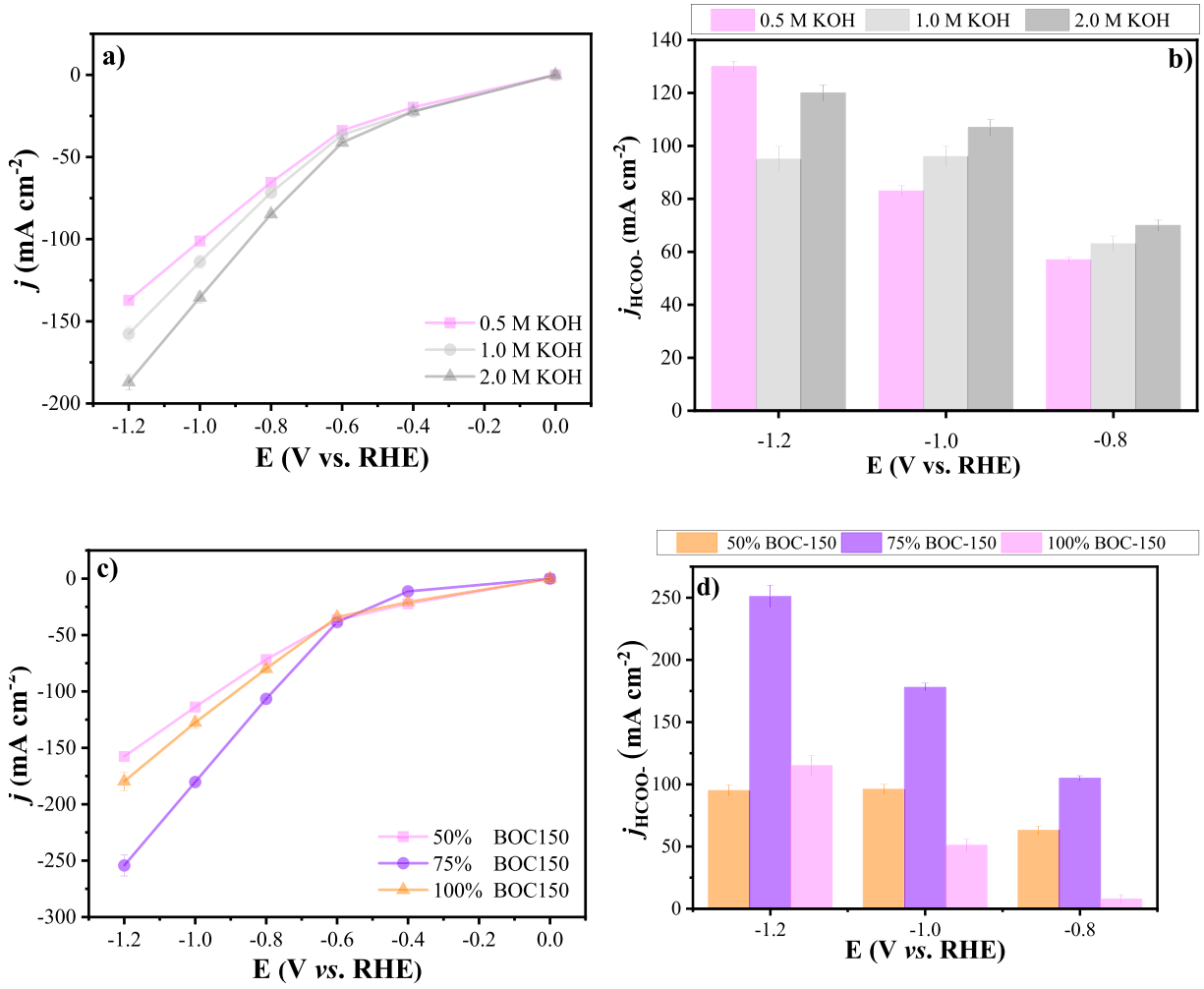

Fig. 7. **(a)** LSV curves and **(b)** FE_{HCOO^-} obtained at different potentials after 30 min using 50% BOC-150 sample evaluated under varying KOH electrolyte concentrations (0.5 M, 1.0 M, and 2.0 M). **(b)** LSV curves and **(d)** FE obtained at different potentials after 30 min using BOC-150 sample with different ratio between catalyst and carbon black (50%, 75%, and 100%).

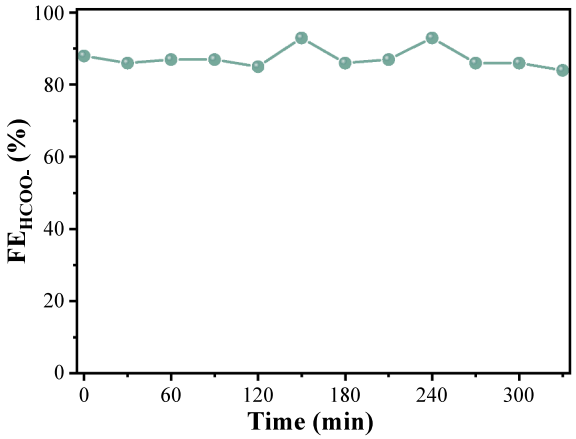

Fig. 8. Chronopotentiometric stability of the BOC150 catalyst at −40 mA in 0.5 M KOH, showing FE_{HCOO^-} over time.

FE_{HCOO^-} higher than 80%. The exceptional performance of the 2D BOC nanosheets, particularly those synthesized under optimized hydrothermal conditions, is attributed to their unique morphological and electronic properties. These properties provide a high density of active sites and significantly facilitate charge transfer, underscoring their considerable potential as advanced electrocatalysts for CO_2 conversion.

CRediT authorship contribution statement

Mateus J. Tomas: Writing – original draft, Methodology, Investigation, Formal analysis. **Daniel R. Sevene:** Writing – original draft, Methodology, Investigation, Formal analysis. **Gonçalves J. Marrenjo:** Writing – original draft, Methodology, Investigation, Formal analysis. **Cleiton P.M. Silva:** Writing – original draft, Methodology, Investigation. **Jessica A. de Oliveira:** Writing – original draft, Supervision, Formal analysis, Data curation. **Caue Ribeiro:** Writing – review & editing, Supervision, Funding acquisition. **Osmando F. Lopes:** Writing – review & editing, Validation, Supervision, Resources, Project administration, Data curation, Conceptualization.

Declaration of competing interest

The authors declare the following financial interests/personal relationships which may be considered as potential competing interests:

Osmando F. Lopes reports financial support was provided by Minas Gerais State Foundation of Support to the Research. Osmando F. Lopes reports financial support was provided by National Council for Scientific and Technological Development. If there are other authors, they declare

that they have no known competing financial interests or personal relationships that could have appeared to influence the work reported in this paper.

Acknowledgments

The authors acknowledge FAPEMIG (Minas Gerais Research Foundation, grant: APQ-00366-24, APQ-05540-25 and APQ-06609-24), CNPq (Brazilian National Council for Scientific and Technological Development, grants: #406026/2023-8, #440117/2022-4), FAPESP (The São Paulo Research Foundation, grant: #2017/11986-5), FINEP (Funding Authority for Studies and Projects, grant: #01.24.0554.00), and Shell #24450-9 (Shell OP001I) - PROEX 23112.001274/2024-30. The authors are grateful to Dr. Jéssica C. Almeida for her valuable assistance with the SEM measurements. In addition, O. F. Lopes is grateful to Dr. Gelson T. S. T. da Silva for the fruitful discussions regarding the stability experiments. The authors would like to acknowledge the Multiuser Laboratories of the Universidade Federal de Uberlândia (RELAM-UFU) for providing the equipment and technical support for experiments involving SEM and XRD (FAPEMIG grant APQ-02391-22).

Supplementary materials

Supplementary material associated with this article can be found, in the online version, at doi:10.1016/j.electacta.2026.148623.

Data availability

Data will be made available on request.

References

[1] Q. Huang, X. Sha, R. Yang, H. Li, J. Peng, Electrochemical conversion of CO2 into formate boosted by In situ reconstruction of Bi-MOF to Bi2O2CO3 ultrathin nanosheets, ACS Appl. Mater. Interfaces 16 (11) (2024) 13882–13892, https://doi.org/10.1021/acsami.4c01120.

[2] B. Zhang, Y. Wu, P. Zhai, C. Wang, L. Sun, J. Hou, Rational design of bismuth-based catalysts for electrochemical CO2 reduction, Chin. J. Catal. 43 (12) (2022) 3062–3088, https://doi.org/10.1016/S1872-2067(22)64132-9.

[3] D. Merum, S.K. Arla, D. Radhalayam, A.M. Tighezza, S.P. Mooni, S.W. Joo, Garland-structured Bi2O2CO3@Ni(OH)2 as a battery-type electrode for high-performance electrochemical energy storage device applications, J. Energy Storage 99 (2024) 113189, https://doi.org/10.1016/j.est.2024.113189.

[4] D. Li, P. Yu, X. Zhou, J.H. Kim, Y. Zhang, P.J.J. Alvarez, Hierarchical Bi2O2CO3 wrapped with modified graphene oxide for adsorption-enhanced photocatalytic inactivation of antibiotic resistant bacteria and resistance genes, Water Res. 184 (2020) 116157, https://doi.org/10.1016/j.watres.2020.116157.

[5] D. Wu, G. Huo, W.Y. Chen, X.Z. Fu, J.L. Luo, Boosting formate production at high current density from CO2 electroreduction on defect-rich hierarchical mesoporous Bi/Bi2O3 junction nanosheets, Appl. Catal. B 271 (January) (2020) 118957, https://doi.org/10.1016/j.apcatb.2020.118957.

[6] B. Ning, Q. Xu, M. Liu, H. Jiang, Y. Hu, C. Li, Bismuthene with stable Bi[Sbnd]O bonds for efficient CO2 electroreduction to formate, Chem. Eng. Sci. 251 (2022) 117409, https://doi.org/10.1016/j.ces.2021.117409.

[7] J. Lee, H. Liu, Y. Chen, W. Li, Bismuth nanosheets derived by in situ morphology transformation of Bismuth oxides for selective electrochemical CO2Reduction to formate, ACS Appl. Mater. Interfaces 14 (12) (2022) 14210–14217, https://doi.org/10.1021/acsami.1c25217.

[8] C. Azenha, C. Mateos-Pedrero, M. Alvarez-Guerra, A. Irabien, A. Mendes, Binary copper-bismuth catalysts for the electrochemical reduction of CO2: study on surface properties and catalytic activity, Chem. Eng. J. 445 (March) (2022), https://doi.org/10.1016/j.cej.2022.136575.

[9] L. Wang, P. Liu, Y. Xu, Y. Zhao, N. Xue, X. Guo, L. Peng, Y. Zhu, M. Ding, Q. Wang, W. Ding, Enhanced catalytic activity and stability of bismuth nanosheets decorated by 3-aminopropyltriethoxysilane for efficient electrochemical reduction of CO2, Appl. Catal. B 298 (July) (2021) 120602, https://doi.org/10.1016/j.apcatb.2021.120602.

[10] Z. Li, B. Sun, D. Xiao, Z. Wang, Y. Liu, Z. Zheng, P. Wang, Y. Dai, H. Cheng, B. Huang, Electron-rich Bi nanosheets promote CO2·− formation for high-performance and PH-universal electrocatalytic CO2 reduction, Angew. Chem. - Int. Ed. 62 (11) (2023), https://doi.org/10.1002/anie.202217569.

[11] B. Ávila-Bolívar, M. Lopez Luna, F. Yang, A. Yoon, V. Montiel, J. Solla-Gullón, S. W. Chee, B. Roldan Cuenya, Revealing the intrinsic restructuring of Bi2O3 nanoparticles into Bi nanosheets during electrochemical CO2 reduction, ACS Appl. Mater. Interfaces 16 (9) (2024) 11552–11560, https://doi.org/10.1021/acsami.3c18285.

[12] H. Qian, Y. Liu, H. Chen, K. Feng, K. Jia, K. Pan, G. Wang, T. Huang, X. Pang, Q. Zhang, Emerging bismuth-based materials: from fundamentals to electrochemical energy storage applications, Energy Storage Mater 58 (2023) 232–270, https://doi.org/10.1016/J.ENSM.2023.03.023.

[13] A. Jayakumar, S. Mathew, S. Radoor, J.T. Kim, J.W. Rhim, S. Siengchin, Recent advances in two-dimensional nanomaterials: properties, antimicrobial, and drug delivery application of nanocomposites, Mater. Today Chem. (2023) 30, https://doi.org/10.1016/j.mtchem.2023.101492.

[14] R. Addou, L. Colombo, Introduction, Defects Two-Dimens. Mater. (2022) 1–5, https://doi.org/10.1016/B978-0-12-820292-0.00007-0.

[15] L. Álvarez, B.R. de Gascue, R.J. Tremont, E. Márquez, E.J. Velazco, Synthesis and characterization of a new aluminum-doped bismuth subcarbonate, Crystals 9 (9) (2019) 9–11, https://doi.org/10.3390/cryst9090466.

[16] M. Wu, Y. Xiong, B. Hu, Z. Zhang, B. Wei, L. Li, J. Hao, W. Shi, Indium doped bismuth subcarbonate nanosheets for efficient electrochemical reduction of carbon dioxide to formate in a wide potential window, J. Colloid Interface Sci. 624 (2022) 261–269, https://doi.org/10.1016/j.jcis.2022.05.054.

[17] C.P.M. Silva, R.A.C. Souza, G.J. Marrenjo, D. Patrun, L. Poggere, S.C. Canobre, S. Mathur, A.O.T. Patrocinio, O.F. Lopes, Boosting electrochemical CO2 to formate conversion via oxygen vacancy-rich 2D SnO2 gas diffusion electrodes, J. Electroanal. Chem. 992 (March) (2025), https://doi.org/10.1016/j.jelechem.2025.119239.

[18] M. Miola, B.C.A. De Jong, P.P. Pescarmona, An efficient method to prepare supported bismuth nanoparticles as highly selective electrocatalyst for the conversion of CO2into formate, Chem. Commun. 56 (95) (2020) 14992–14995, https://doi.org/10.1039/d0cc06818g.

[19] A. Peterson, J. Nørskov, Activity descriptors for CO2 electroreduction to methane on transition metal catalysts, J. Phys. Chem. Lett. 3 (2) (2012) 251–258, https://doi.org/10.1021/jz201461p.

[20] X. Cao, B. Wulan, Y. Wang, J. Ma, S. Hou, J. Zhang, Atomic bismuth induced ensemble sites with indium towards highly efficient and stable electrocatalytic reduction of carbon dioxide, Sci. Bull. (Beijing) 68 (10) (2023) 1008–1016, https://doi.org/10.1016/j.scib.2023.04.026.

[21] D. Xia, R. Xie, H. Xie, Y. Pang, P. Huang, G. He, G. Chai, Halide precursor reduction strategy to modulate bismuthene with high selectivity and wide potential window for electrochemical CO2 reduction, AIChE J. 70 (5) (2024) 1–13, https://doi.org/10.1002/aic.18389.

[22] J. Zeng, N.B.D. Monti, T. Chen, M. Castellino, W. Ju, M.A.O. Lourenço, P. Jagdale, C.F. Pirri, Evolution of bismuth electrodes activating electrosynthesis of formate from carbon dioxide reduction, Catal. Today 437 (March) (2024), https://doi.org/10.1016/j.cattod.2024.114743.

[23] S. Liu, B. Hu, J. Zhao, W. Jiang, D. Feng, C. Zhang, W. Yao, Enhanced electrocatalytic CO2 reduction of bismuth nanosheets with introducing surface bismuth subcarbonate, Coatings 12 (2) (2022), https://doi.org/10.3390/coatings12020233.

[24] M.B. Ross, P. De Luna, Y. Li, C.-T.T. Dinh, D. Kim, P. Yang, E.H. Sargent, Designing materials for electrochemical carbon dioxide recycling, Nat. Catal. 2 (8) (2019) 648–658, https://doi.org/10.1038/s41929-019-0306-7.

[25] M.F. Baruch, J.E. Pander, J.L. White, A.B. Bocarsly, Mechanistic insights into the reduction of CO2 on tin electrodes using in situ ATR-IR spectroscopy, ACS Catal. 5 (5) (2015) 3148–3156, https://doi.org/10.1021/acscatal.5b00402.

[26] C. Lin, Y. Liu, X. Kong, Z. Geng, J. Zeng, Electrodeposited highly-oriented bismuth microparticles for efficient CO2 electroreduction into formate, Nano Res. 15 (12) (2022) 10078–10083, https://doi.org/10.1007/s12274-022-4345-z.

[27] J. Zhang, Z. Liu, Z. Ma, Facile formation of Bi 2 O 2 CO 3 /Bi 2 MoO 6 nanosheets for visible light-driven photocatalysis, ACS Omega 4 (2) (2019) 3871–3880, https://doi.org/10.1021/acsomega.8b03699.

[28] J. Yang, X. Wang, Y. Qu, X. Wang, H. Huo, Q. Fan, J. Wang, L.M. Yang, Y. Wu, Bi-based metal-organic framework derived leafy bismuth nanosheets for carbon dioxide electroreduction, Adv. Energy Mater. 10 (36) (2020) 1–7, https://doi.org/10.1002/aenm.202001709.

[29] Q. Zhao, J. Wang, Y. Zhuang, L. Gong, W. Zhang, W. Fan, Z. Lu, Y. Zhang, T. Fujita, P. Zhang, Q.In Xue, Situ reconstruction of Bi nanoparticles confined within 3D nanoporous Cu to boost CO2 electroreduction, Sci. China Mater. 67 (3) (2024) 796–803, https://doi.org/10.1007/s40843-023-2753-4.

[30] M. Luo, Z. Wang, Y.C. Li, J. Li, F. Li, Y. Lum, D.H. Nam, B. Chen, J. Wicks, A. Xu, T. Zhuang, W.R. Leow, X. Wang, C.T. Dinh, Y. Wang, Y. Wang, D. Sinton, E. H. Sargent, Hydroxide promotes carbon dioxide electroreduction to ethanol on copper via tuning of adsorbed hydrogen, Nat. Commun. 10 (1) (2019) 1–7, https://doi.org/10.1038/s41467-019-13833-8.

[31] Weekes, D.M.; Salvatore, D.A.; Reyes, A.; Huang, A.; Berlinguette, C.P. Electrolytic CO 2 reduction in a flow cell. 2018. https://doi.org/10.1021/acs.accounts.8b00010.

[32] Y. Yuan, Q. Wang, Y. Qiao, X. Chen, Z. Yang, W. Lai, T. Chen, G. Zhang, H. Duan, M. Liu, H.In Huang, Situ structural reconstruction to generate the active sites for CO2 electroreduction on bismuth ultrathin nanosheets, Adv. Energy Mater 12 (29) (2022) 1–8, https://doi.org/10.1002/aenm.202200970.

[33] I. Zelocualtecatl Montiel, A. Dutta, K. Kiran, A. Rieder, A. Iarchuk, S. Vesztergom, M. Mirolo, I. Martens, J. Drnec, P. Broekmann, CO2Conversion at high current densities: stabilization of Bi(III)-containing electrocatalysts under CO2Gas flow conditions, ACS Catal. 12 (17) (2022) 10872–10886, https://doi.org/10.1021/acscatal.2c02549.

[34] H. Zheng, G. Wu, G. Gao, X. Wang, The bismuth architecture assembled by nanotubes used as highly efficient electrocatalyst for CO2 reduction to formate,

Chem. Eng. J. 421 (P1) (2021) 129606, https://doi.org/10.1016/j.cej.2021.129606.
[35] W. Lv, J. Bei, R. Zhang, W. Wang, F. Kong, L. Wang, W. Wang, Bi2O2CO3 Nanosheets as electrocatalysts for selective reduction of CO2 to formate at low overpotential, ACS Omega 2 (6) (2017) 2561–2567, https://doi.org/10.1021/acsomega.7b00437.
[36] O.F. Lopes, K.T.G. Carvalho, W. Avansi, D.M.B. Milori, C. Ribeiro, Insights into the photocatalytic performance of Bi2O2CO3/BiVO4 heterostructures prepared by one-step hydrothermal method, RSC Adv. 8 (20) (2018) 10889–10897, https://doi.org/10.1039/c8ra00605a.
[37] X.Du Liang, Q.Z. Zheng, N. Wei, Y.Y. Lou, S.N. Hu, K.M. Zhao, H.G. Liao, N. Tian, Z.Y. Zhou, S.G Sun, In-situ constructing Bi@Bi2O2CO3 nanosheet catalyst for ampere-level CO2 electroreduction to formate, Nano Energy 114 (June) (2023) 108638, https://doi.org/10.1016/j.nanoen.2023.108638.
[38] Y. Huang, W. Wang, Q. Zhang, J.J. Cao, R.J. Huang, W. Ho, S.C.In Lee, Situ fabrication of α-Bi2O3/(BiO)2CO3 nanoplate heterojunctions with tunable optical property and photocatalytic activity, Sci. Rep. 6 (November 2015) (2016) 1–9, https://doi.org/10.1038/srep23435.
[39] P. Kar, T.K. Maji, R. Nandil, P. Lemmens, S.K. Pal, In-situ hydrothermal synthesis of Bi-Bi2O2CO3 heterojunction photocatalyst with enhanced visible light photocatalytic activity, Nanomicro Lett. 9 (2) (2017), https://doi.org/10.1007/s40820-016-0118-0.
[40] T. Gupta, N. Rosza, M. Sauer, A. Goetz, M. Winzely, J. Rath, S. Naghdi, A. Lechner, D.H. Apaydin, A. Cherevan, G. Friedbacher, A. Foelske, S.M. Skoff, B.C. Bayer, D. Eder, Sonochemical synthesis of large two-dimensional Bi2O2CO3 nanosheets for hydrogen evolution in photocatalytic water splitting, Adv. Sustain. Syst. 6 (11) (2022) 1–8, https://doi.org/10.1002/adsu.202100326.
[41] C. Yu, W. Zhou, L. Zhu, G. Li, K. Yang, R. Jin, Integrating plasmonic Au nanorods with dendritic like α-Bi2O3/Bi2O2CO3 heterostructures for superior visible-light-driven photocatalysis, Appl. Catal. B 184 (2016) 1–11, https://doi.org/10.1016/j.apcatb.2015.11.026.
[42] G. Zhu, S. Li, J. Gao, F. Zhang, C. Liu, Q. Wang, M. Hojamberdiev, Constructing a 2D/2D Bi2O2CO3/Bi4O5Br2 heterostructure as a direct Z-scheme photocatalyst with enhanced photocatalytic activity for NOx removal, Appl. Surf. Sci. 493 (July) (2019) 913–925, https://doi.org/10.1016/j.apsusc.2019.07.119.
[43] D.M.R. de Rooij, Electrochemical methods: fundamentals and applications, Anti-Corros. Methods Mater. 50 (5) (2003), https://doi.org/10.1108/acmm.2003.12850eae.001.
[44] L.A.J. Garvie, L. Trif, D. Cotto-Figueroa, E. Asphaug, C.G. Hoover, High surface area and interconnected nanoporosity of clay-rich astromaterials, Sci. Rep. 14 (1) (2024) 1–11, https://doi.org/10.1038/s41598-024-61114-2.
[45] W. Zuo, M. Qi, Y. Liu, H. Li, H. Han, Y. Wang, L. Long, S. Wu, Study on gas adsorption-desorption and diffusion behaviour in coal pores modified by nano fracturing fluid, ACS Omega 8 (32) (2023) 29213–29224, https://doi.org/10.1021/acsomega.3c02227.
[46] C. Schlumberger, M. Thommes, Characterization of hierarchically ordered porous materials by physisorption and mercury porosimetry—A tutorial review, Adv. Mater. Interfaces 8 (4) (2021), https://doi.org/10.1002/admi.202002181.
[47] V.G. Baldovino-Medrano, V. Niño-Celis, R. Isaacs Giraldo, Systematic analysis of the nitrogen adsorption-desorption isotherms recorded for a series of materials based on microporous-mesoporous amorphous aluminosilicates using classical methods, J. Chem. Eng. Data 68 (9) (2023) 2512–2528, https://doi.org/10.1021/acs.jced.3c00257.
[48] Y. Wang, X. Zhu, Y. Li, Spin-orbit coupling-dominated catalytic activity of two-dimensional bismuth toward CO2 electroreduction: not the thinner the better, J. Phys. Chem. Lett. 10 (16) (2019) 4663–4667, https://doi.org/10.1021/acs.jpclett.9b01406.
[49] T. Burdyny, W.A. Smith, CO2 Reduction on gas-diffusion electrodes and why catalytic performance must Be assessed at commercially-relevant conditions, Energy Env. Sci. 12 (5) (2019) 1442–1453, https://doi.org/10.1039/c8ee03134g.
[50] Y. Hori, H. Wakebe, T. Tsukamoto, O. Koga, Electrocatalytic process of CO selectivity in electrochemical reduction of CO2 at metal electrodes in aqueous Media, Electrochim. Acta 39 (11–12) (1994) 1833–1839, https://doi.org/10.1016/0013-4686(94)85172-7.
[51] Ren, S.; Joulié, D.; Salvatore, D.; Torbensen, K.; Wang, M.; Robert, M.; Berlinguette, C.P. Molecular electrocatalysts can mediate fast, selective CO 2 reduction in a flow cell. 2019, 369 (July), 367–369.
[52] J. Xu, Z. Meng, Z. Hao, X. Sun, H. Nan, H. Liu, Y. Wang, W. Shi, H. Tian, X. Hu, Oxygen-vacancy abundant alpha bismuth oxide with enhanced cycle stability for high-energy hybrid supercapacitor electrodes, J. Colloid Interface Sci. 609 (2022) 878–889, https://doi.org/10.1016/J.JCIS.2021.11.081.
[53] A. He, C. Wang, N. Zhang, Z. Wen, Y. Ma, G. Yan, R. Xue, Oxygen vacancy-rich CeOx-Bi2O2CO3 nanosheets for enhancing electrocatalytic reduction of CO2 to formate, Appl. Surf. Sci. 638 (July) (2023), https://doi.org/10.1016/j.apsusc.2023.158140.
[54] S. Wu, M. He, M. Yang, B. Zhang, F. Wang, Q. Li, Near-infrared spectroscopy study of serpentine minerals and assignment of the Oh group, Crystals 11 (9) (2021) 1–11, https://doi.org/10.3390/cryst11091130.
[55] J.A. Torres, A.E. Nogueira, G.T.S.T. da Silva, C. Ribeiro, The effect of SnO2 surface properties on CO2 photoreduction to higher hydrocarbons, ChemCatChem 15 (6) (2023) 1–9, https://doi.org/10.1002/cctc.202201534.
[56] D.A. Popescu, J.M. Herrmann, A. Ensuque, F. Bozon-Verduraz, Nanosized tin dioxide: spectroscopic (UV-VIS, NIR, EPR) and electrical conductivity studies, Phys. Chem. Chem. Phys. 3 (12) (2001) 2522–2530, https://doi.org/10.1039/b100553g.
[57] R.L. Frost, É. Makó, J. Kristóf, J.T. Kloprogge, Modification of kaolinite surfaces through mechanochemical treatment - A mid-IR and near-IR spectroscopic study, Spectrochim. Acta Mol. Biomol. Spectrosc 58 (13) (2002) 2849–2859, https://doi.org/10.1016/S1386-1425(02)00033-1.
[58] G.J. Marrenjo, G.T.S.T. da Silva, R.A.A. Muñoz, L.H. Mascaro, O.F. Lopes, Modification of ZnO gas-diffusion-electrodes for enhanced electrochemical CO2 reduction: optimization of operational conditions and mechanism investigation, Mater. Adv. 5 (23) (2024) 9231–9242, https://doi.org/10.1039/d4ma00750f.
[59] M. Ramdin, A.R.T. Morrison, M. De Groen, R. Van Haperen, R. De Kler, L.J.P. Van Den Broeke, J.P. Martin Trusler, W. De Jong, T.J.H Vlugt, High pressure electrochemical reduction of CO2 to formic acid/formate: a comparison between bipolar membranes and cation exchange membranes, Ind. Eng. Chem. Res. 58 (5) (2019) 1834–1847, https://doi.org/10.1021/acs.iecr.8b04944.
[60] A. Kas, P. Izadi, F. Harnisch, High salt electrolyte solutions challenge the electrochemical CO2 reduction reaction to formate at indium and tin cathodes, ChemElectroChem 10 (23) (2023) 1–8, https://doi.org/10.1002/celc.202300311.
[61] M. Rodrigues Pinto, R.E. Vos, R. Nagao, M.T.M. Koper, Electrolyte effects on electrochemical CO2 reduction reaction at Sn metallic electrode, J. Phys. Chem. C 128 (50) (2024) 21421–21429, https://doi.org/10.1021/acs.jpcc.4c06361.
[62] S.D. Verma, S.A. Corcelli, M.A. Berg, Rate and amplitude heterogeneity in the solvation response of an ionic liquid, J. Phys. Chem. Lett. 7 (3) (2016) 504–508, https://doi.org/10.1021/acs.jpclett.5b02835.
[63] R. Kas, K.K. Hummadi, R. Kortlever, P. De Wit, A. Milbrat, M.W.J. Luiten-Olieman, N.E. Benes, M.T.M. Koper, G. Mul, Three-dimensional porous hollow fibre copper electrodes for efficient and high-rate electrochemical carbon dioxide reduction, Nat. Commun. (2016) 7, https://doi.org/10.1038/ncomms10748.
[64] C. Dinh, T. Burdyny, G. Kibria, A. Seifitokaldani, C.M. Gabardo, F.P.G.de Arquer, A. Kiani, J.P. Edwards, P.De Luna, O.S. Bushuyev, C. Zou, R. Quintero-Bermudez, Y. Pang, D. Sinton, E.H Sargent, Sustained high-selectivity CO 2 electroreduction to ethylene via hydroxide-mediated catalysis at an abrupt reaction interface. Submitted to, Sci. (1979) 787 (May) (2018) 783–787.
[65] S. Garg, M. Li, A.Z. Weber, L. Ge, L. Li, V. Rudolph, G. Wang, T.E. Rufford, Advances and challenges in electrochemical CO2 reduction processes: an engineering and design perspective looking beyond new catalyst materials, J. Mater. Chem. A. R. Soc. Chem. (2020) 1511–1544, https://doi.org/10.1039/c9ta13298h.
[66] C.M. Gabardo, A. Seifitokaldani, J.P. Edwards, C.T. Dinh, T. Burdyny, M.G. Kibria, C.P. O'Brien, E.H. Sargent, D. Sinton, Combined high alkalinity and pressurization enable efficient CO2 electroreduction to CO, Energy Env. Sci. 11 (9) (2018) 2531–2539, https://doi.org/10.1039/c8ee01684d.
[67] Kim, S.; Doh, Y.; Oh, J.; Tae, K. Hydrophobic carbon nanotube-PTFE network in gas diffusion electrode for flooding resistance in CO 2 electroreduction. 2025, 22–26. https://doi.org/10.1002/cssc.202501694.